Strontium Oxide Tunnel Barriers for High Quality Spin Transport and Large Spin Accumulation in Graphene

Simranjeet Singh,[†,‖] Jyoti Katoch,[†,‖] Tiancong Zhu,[†] Ryan J. Wu,[‡] Adam S. Ahmed,[†] Walid Amamou,[§] Dongying Wang,[†] K. Andre Mkhoyan,[‡] and Roland K. Kawakami*,[†,§]

[†]Department of Physics, The Ohio State University, Columbus, Ohio 43210, United States

[‡]Department of Chemical Engineering and Materials Science, University of Minnesota, Minneapolis, Minnesota 55455, United States

[§]Program of Materials Science and Engineering, University of California, Riverside, California 92521, United States

S *Supporting Information*

ABSTRACT: The quality of the tunnel barrier at the ferromagnet/graphene interface plays a pivotal role in graphene spin valves by circumventing the impedance mismatch problem, decreasing interfacial spin dephasing mechanisms and decreasing spin absorption back into the ferromagnet. It is thus crucial to integrate superior tunnel barriers to enhance spin transport and spin accumulation in graphene. Here, we employ a novel tunnel barrier, strontium oxide (SrO), onto graphene to realize high quality spin transport as evidenced by room-temperature spin relaxation times exceeding a nanosecond in graphene on silicon dioxide substrates. Furthermore, the smooth and pinhole-free SrO tunnel barrier grown by molecular beam epitaxy (MBE), which can withstand large charge injection current densities, allows us to experimentally realize large spin accumulation in graphene at room temperature. This work puts graphene on the path to achieve efficient manipulation of nanomagnet magnetization using spin currents in graphene for logic and memory applications.

KEYWORDS: *Graphene spintronics, tunnel barrier, molecular beam epitaxy, spin current and spin accumulation, lateral spin valves, transmission electron microscopy*
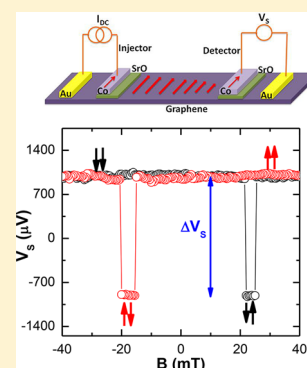
Spins can be used to efficiently control/manipulate the magnetization of nanomagnets for logic and memory applications. This requires generation of high spin current density, its long-distance transport, and subsequent detection. Graphene has already been a promising candidate as a spin channel material for next generation spintronic devices owing to the large spin diffusion lengths and long spin relaxation times at room temperature.[1] However, the realization of large spin current densities, required for manipulating and controlling the nanomagnetic bits by spin torque,[2] remains elusive in graphene spin channels. Out of the many experimental techniques,[3,4] electrical spin injection is the most common and efficient way to generate pure spin currents in graphene.[1,5] A charge current flowing from a ferromagnet (injector) into graphene generates a spin accumulation at the interface,[6] which decays laterally in the graphene channel and subsequently can be detected by another ferromagnetic electrode detector.[1] The amplitude of the nonlocal voltage signal at the detector, that is, the difference of the measured voltage for parallel and antiparallel magnetization of injector and detector electrodes, is directly proportional to the spin accumulation in graphene.[7] Tunnel barriers at the ferromagnet/graphene interface play a crucial role to circumvent the impedance mismatch problem as well as decrease the spin absorption by the ferromagnet,[8,9] which helps enhance the spin accumulation in graphene.[10] Studies have reported spin accumulation up to a few millielectronvolts in few-micron long graphene spin channels.[11−16] This spin accumulation is most likely limited by nonuniformities of the barriers that contribute to their electric breakdown.

In this Letter, we employ a novel tunnel barrier, strontium oxide (SrO), onto graphene to realize high quality spin transport and large spin accumulation signals in graphene. Smooth and pinhole-free SrO tunnel barriers grown by MBE, which can withstand charge injection current densities as large as ~10^{10} A/m², allow us to experimentally realize large spin accumulation in graphene. In lateral graphene spin valve devices with few micron long graphene spin channels, we observe nonlocal spin voltages of ΔV_S = 1.8 mV at room temperature, which corresponds to a spin accumulation in graphene of μ_S = 7.5 meV underneath the spin detector. As shown in Table 1, 7.5 meV is the largest value reported to date for graphene. Transmission electron microscopy (TEM) images recorded from cross sections of functional devices show that the SrO layers on graphene have smooth morphology, no detectable pinholes, and predominantly amorphous structure (some small crystalline grains might still be present). Additionally, measurements with various interfacial contact resistance of the ferromagnet/graphene injector interface show that intermediate contact resistances are better at achieving large spin accumulation as compared to high

Table 1. Comparison of Spin Accumulation and Spin Currents for Various Barriers

barrier	geometry	bias current	injector/detector polarization	injected dc spin current	injector-detector distance	measured dc spin voltage ΔV_S	spin accumulation in graphene at detector, $\mu_s{}^a$	ref
SrO	nonlocal	250 μA	0.116	29 μA	1.8 μm	1.8 mV	7.5 meV	this work
amorphous Carbon	nonlocal	46 μA	0.10–0.15	4.6–6.9 μA	1.15 μm	0.5 mV	1.5–2.5 meV	13
h-BN	nonlocal	25 μA	p_{INJ}, −0.70 to +0.40; p_{DET}, 0.013	9 μA^b	1 μm	0.05 mV^c	2 meV	16
fluorinated graphene	nonlocal	150 μA	high bias, 0.35; low bias, 0.63	53 μA	5.75 μm	0.07 mV	0.1 meV	14
Ti-seeded MgO	nonlocal	15 μA	0.11	1.6 μA^b	1.8 μm	0.06 mV^c	0.25 meV	15
Al$_2$O$_3$ with pinholes	nonlocal	5 μA	0.18–0.31	1.2 μA^b	2 μm	0.35 mV^c	0.7 meV	12
no barrier (Co/graphene)	nonlocal	V_{bias} = +2.7 V			1.5 μm	0.17 mV		11
metallic LSV (NiFe/MgO/Ag)	nonlocal	3.5 mA^d	p_{INJ} = 0.42; p_{DET} = 0.30	1.5 mA^d	0.3 μm	0.22 mV^d	0.36 meV^d	25
h-BN	2T local	20 μA	p_{INJ}, −0.50 to +0.30; p_{DET}, −0.70 to +1.30	5 μA (inj)^b 13 μA (det)^b	1 μm	7 mV	4.1 meV	16
fluorinated graphene	single interface Hanle	150 μA	high bias, 0.35; low bias, 0.63	53 μA		1.7 mV	5 meV	14

^{a}For nonlocal measurements, the absolute spin accumulation is $\mu_s = (\mu_{\uparrow\uparrow} - \mu_{\downarrow\uparrow})/2$. ^{b}For ac lock-in measurements, the injected dc spin current is estimated according to $I_S^{dc} = P^{dc}I^{dc} = \int_0^{I^{dc}} p^{ac}(I)\,dI$, where $p^{ac}(I)$ is the bias dependent differential (ac) spin polarization. ^{c}For ac lock-in measurements, the dc spin voltage is estimated by integrating the differential (ac) nonlocal magnetoresistance. ^{d}Measurements are taken using short current pulses (200 μs) and synchronized voltage measurements.
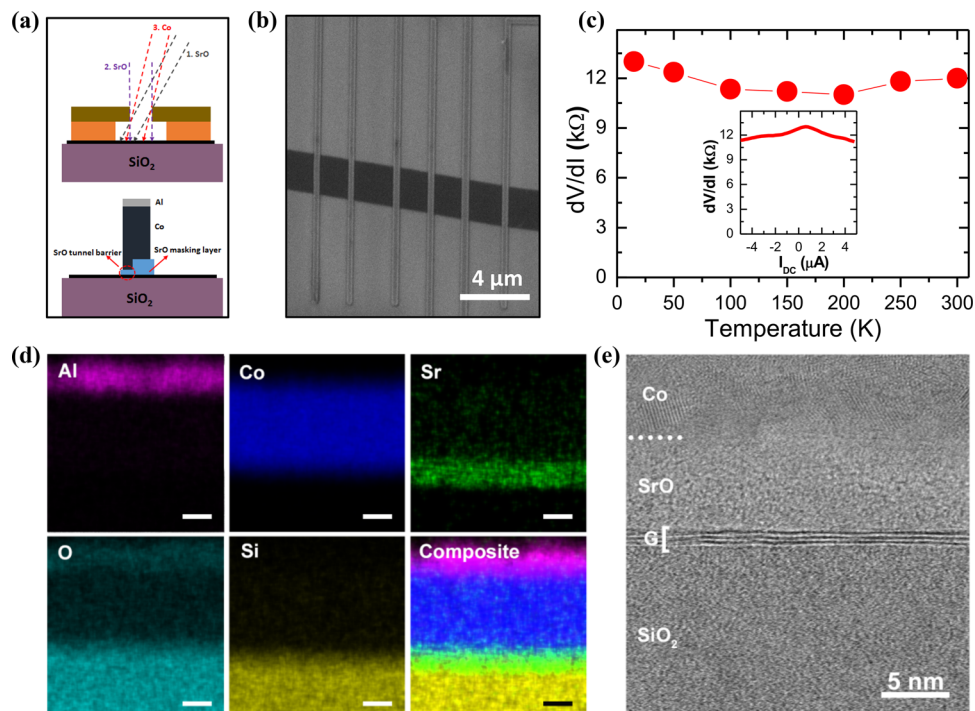

Figure 1. (a) Schematic showing the angle evaporation geometry used for defining SrO tunnel barriers onto graphene. (b) SEM image of a completed graphene lateral spin valve device with multiple electrodes. (c) The temperature dependence of the zero-bias contact resistance of a typical electrode (red filled circles). Inset: the differential contact resistance of the electrode as a function of bias current measured at 15 K. (d) STEM-EDX measurements showing elemental maps for aluminum (capping layer), cobalt, strontium, oxygen, and silicon, and a composite map of all elements except oxygen. The scale bars are 20 nm. (e) High-resolution BF-STEM cross-sectional image of a graphene/SrO/Co junction. Each layer of the junction is labeled.

resistance (due to electric breakdown of tunnel barrier at relatively lower charge injection currents) or low resistance (due to reduced spin injection efficiency because of the conductance mismatch problem).[1] Our work establishes that in comparison to other tunnel barriers that we have utilized including Ti-seeded MgO,[10] Al$_2$O$_3$,[17] and h-BN,[18] SrO provides a better combination of durability, large spin accumulation, spin injection efficiency, ease of fabrication, and device yield that makes SrO an attractive new tunnel barrier for graphene spin valve devices. Moreover, experimental advances presented in this work are crucial for memory and spin-logic applications
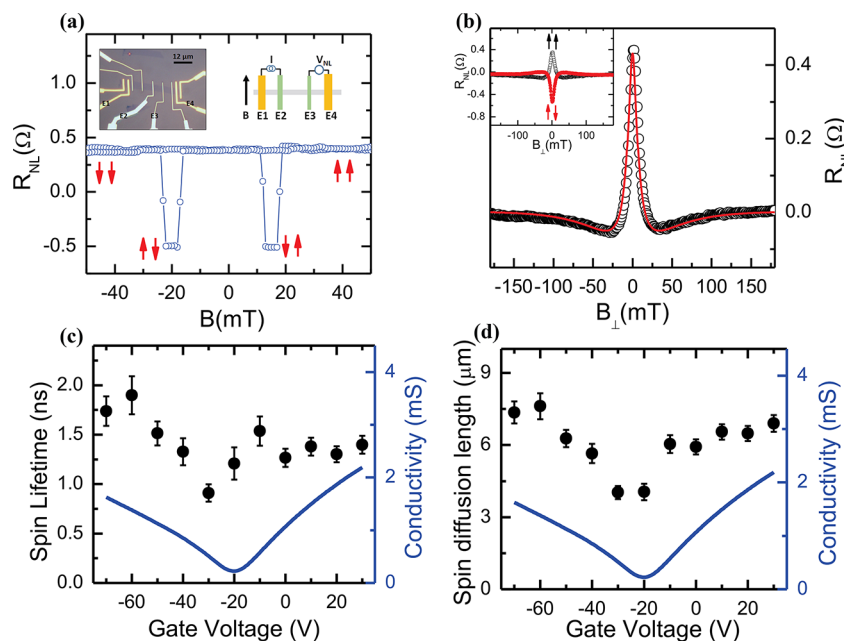
Figure 2. Room-temperature spin transport in single layer graphene using SrO tunnel barriers (a) Nonlocal magneto-resistance (MR) signal measured in a graphene spin valve using E2 and E3 as injector and detector electrodes. The red arrows depict the relative magnetization direction of injector and detector electrodes. Inset: the optical micrograph of the device and schematic of the nonlocal measurement. (b) Nonlocal Hanle spin precession curve (black circles) obtained by subtracting parallel and antiparallel Hanle curves from inset to panel b. The thick red line is the fit to the data to extract the spin relaxation time (τ_s). Inset: Nonlocal Hanle spin precession signal measured in parallel (black circles) and antiparallel (red circles) configuration. (c) The gate dependence of the fitted spin relaxation times (black filled circles) over a range of applied back gate voltages. The corresponding graphene conductivity as a function of back gate voltage is shown by solid blue curve. (d) Extracted spin diffusion length for graphene as a function of applied back gate voltage, wherein the solid blue curve is the gate dependent graphene conductivity.

that require large spin current densities to manipulate the magnetization state of nanomagnetic data bits.[2]

Devices are fabricated using exfoliated monolayer or few-layer graphene sheets on SiO_2/Si substrate (300 nm thick SiO_2). The Si substrate is degenerately doped and used as a back gate. Electrodes are patterned with standard electron-beam lithography using PMMA/MMA bilayer resist to produce an undercut for angle evaporation.[10] The SrO tunnel barriers are grown by angle evaporation in a MBE chamber as schematically shown in Figure 1a. Strontium is deposited from an effusion cell at rate of 3 Å/min in the presence of molecular oxygen (with partial pressure of 2.4×10^{-7} Torr) until a thin SrO tunnel barrier (0.7−1 nm) is grown. Subsequently, a thick masking layer of SrO (∼4 nm) is grown at a different angle as depicted in Figure 1a. Additional in situ oxidation for 3 h at the same oxygen partial pressure is also carried out to further oxidize the Sr. Then, 80 nm cobalt is deposited, which is further capped by a few nanometers of aluminum to avoid oxidation of Co. It is worth noting that using angle evaporations, as shown in Figure 1a, reduces the effective area through which electrons can tunnel from Co to graphene (∼50 nm width). A scanning electron microscopy (SEM) image of a completed graphene spin valve (GSV) device with multiple Co electrodes is shown in Figure 1b.

In order to electrically characterize the SrO tunnel barriers on graphene, we measure the interfacial contact resistance using a 3-probe configuration, wherein the differential contact resistance (dV/dI) is recorded as a function of dc bias current.[6] The dV/dI curves exhibit a typical peak at zero dc current bias as expected for a tunnel barrier. The measured dV/dI data for a typical Co/SrO/graphene interface (at 15 K) is shown in the inset to the Figure 1c. The values of zero bias dV/dI as a

function of the temperature are plotted in Figure 1c. One can clearly notice the very weak temperature dependence of the contact resistance, which is often considered a signature of good pinhole-free tunnel barrier. Although not shown, we note that by varying the thickness of SrO between 0.7 and 1 nm, the contact resistance varies from a few kilo-ohms (kΩ) to tens of kΩ, along with some sample-to-sample variation under nominally identical conditions is smaller compared to Ti-seeded MgO barriers.[6]

To characterize the interfacial structure of the SrO tunnel barrier, TEM cross-sectional lamellas from functioning GSVs are prepared using a focused ion beam (FIB) and subsequently studied using scanning-TEM (STEM). For this analysis, an aberration-corrected FEI Titan G2 60-300 STEM equipped with a Super-X energy dispersive X-ray (EDX) spectrometer is used and operated at 200 keV.[19] Figure 1d shows low-magnification STEM-EDX elemental maps of the sample in which each layer of the cross-sectionally cut GSV can be chemically identified. Figure 1e shows a high-magnification bright-field STEM (BF-STEM) image of the Co/SrO/graphene/a-SiO_2 interfaces where the few-layer graphene (∼4 layers) is visible. The interfaces appear to be smooth. The BF-STEM image shows that the Co layer is polycrystalline as demonstrated by the various crystalline grains with different orientations. In contrast, the SrO layer appears to be predominantly amorphous. The amorphous structure is somewhat surprising given our previous observation of (001) textured growth of SrO thin films on HOPG substrates as well as on epitaxial graphene on SiC(0001),[20] but the conditions for growth and postprocessing are different during graphene spin valve fabrication. We believe that the amorphous structure of SrO, which is free of grain boundaries found in polycrystalline
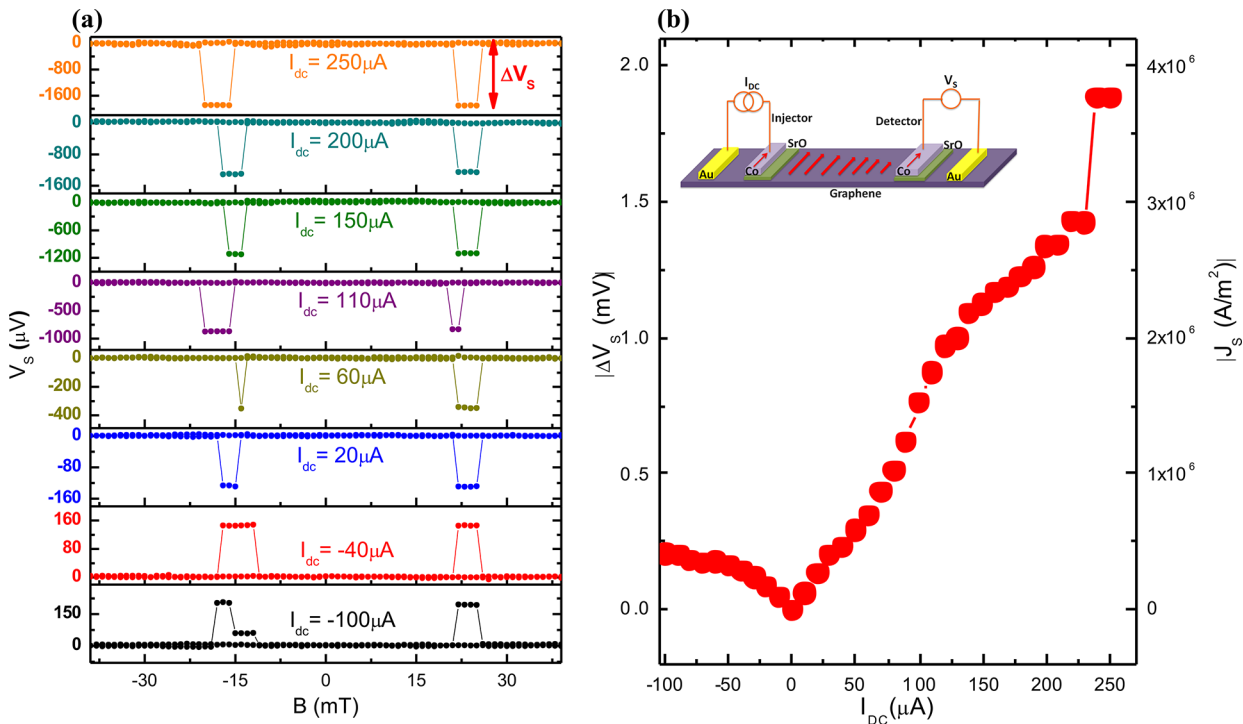
Figure 3. Room-temperature dc spin accumulation measurement in single layer graphene employing SrO tunnel barriers (a) Nonlocal dc spin accumulation signal measured as a function of applied field at a fixed bias. From bottom to top, the nonlocal signals for increasing applied dc currents. The double red arrow shows the magnitude of the spin accumulation signal at a fixed applied current bias. (b) The magnitude of the measured spin accumulation signal (left axis), shown by red filled circles, as a function of applied charge injection current. On the right axis is the calculated spin current density (corresponding to nonlocal spin accumulation voltage) as a function of applied current bias at the injector. The graphene channel length in this particular device is 1.8 μm.

films, as well as the smooth film morphology contribute to the robustness that the SrO barriers display under high current density and, in turn, allows us to realize large spin accumulation as discussed later. Additionally, STEM studies of SrO tunnel barriers on graphene do not show any obvious pinholes, which is consistent with the differential conductance measurements of graphene/SrO interfaces showing good tunneling characteristics.

Next, we study the spin transport in GSVs with SrO tunnel barriers. Here we report the detailed spin transport at 300 K from a single layer GSV out of the many devices that we have measured (more than 10 with graphene thickness varying from 1 to 4 layers). An optical micrograph of this device is shown in the left inset in Figure 2a. For the data presented here, the single layer graphene channel length is 6 μm and width is 2 μm. We intentionally use a longer graphene channel length to ensure the values of spin relaxation time and spin diffusion length as extracted from one-dimensional spin diffusion model are not underestimated.[17,21] The nonlocal magnetoresistance (MR) measurements are performed using low frequency (11 Hz) ac current excitation of 1 μA rms. As shown in the right inset in Figure 2a, ac spin injection current excitation is applied between the injector electrode and graphene, and a nonlocal voltage signal is measured using the detector electrode and graphene. An external magnetic field is swept along the electrode's length, and a nonlocal voltage signal is recorded as a function of the applied magnetic field magnitude. Figure 2a shows the observed nonlocal MR signal. The nonlocal resistance (R_{NL}) is obtained by dividing the voltage signal by the magnitude of applied current (1 μA). At approximately ±15 mT, we see an abrupt change in R_{NL} when the relative

magnetization directions of the injector and detector electrodes changes to the antiparallel state. By further increasing the magnetic field, the resistance signal again changes back to the original value due to the alignment of the injector and detector magnetizations back to a parallel state. Similarly, while sweeping with a decreasing magnetic field, a sharp change in MR occurs on the negative magnetic field side. The red arrows in Figure 2a indicate the relative alignment of the injector/detector magnetizations during the magnetic field sweeps. This MR curve is the hallmark of nonlocal spin transport along a nonmagnetic spin channel.[1]

To measure the spin relaxation times in GSV employing SrO tunnel barriers, we perform nonlocal Hanle spin precession measurements.[1] In Hanle precession measurements, the injected spins with in-plane polarization precess under the influence of an externally applied out-of-plane magnetic field. For either a parallel or antiparallel configuration of the injector and detector electrodes, the nonlocal resistance signal is measured as a function of the applied magnetic field perpendicular to the plane of the graphene device. The inset of Figure 2b shows the Hanle curves obtained for the GSV measured in parallel (black circles) and antiparallel (red circles) configuration. The measured data for parallel and antiparallel configurations are subtracted to obtain the curve in Figure 2b (black circles). As explained in the Supporting Information, we fit our nonlocal Hanle data using an analytical solution to the steady state Bloch equation developed by Sosenko et al.[22] The experimentally obtained Hanle curves (as in Figure 2b) can be fit using spin relaxation time (τ_s), spin diffusion length in graphene (λ), and the product of injector and detector spin polarizations ($p_{inj}p_{det}$) as the fitting parameters. The fit for the
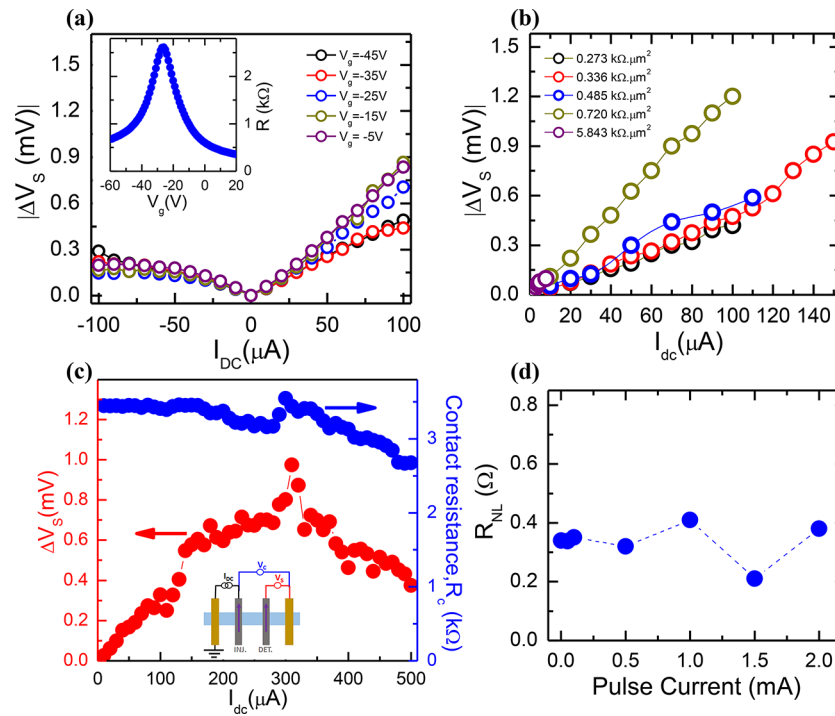
Figure 4. (a) Bias dependence of the spin accumulation signals for a single layer GSV (channel length ~2 μm) at various applied gate voltages is shown by different colored circles. Bias dependence at each gate voltage is color coded as depicted. Inset: graphene channel resistance as a function of applied gate voltage. (b) Bias dependence of the spin accumulation measured for different single layer graphene devices (channel length ~2 μm) having injector electrodes with interfacial contact resistance area (RA) product varying from 0.273 to 5.843 k$\Omega \cdot \mu$m^2. (c) The simultaneous measurement of bias dependent spin accumulation signals and the interfacial contact resistance of the injector electrode. The spin accumulation (as a function of bias current) is shown by red filled circles (left axis). At each applied bias current, the interfacial contact resistance is measured and shown by blue filled circles. Inset: schematic of the simultaneous measurement scheme for spin accumulation and injector interfacial contact resistance. (d) Nonlocal MR signal measured in a few-layer graphene (3 or 4) spin valve after applying increasing magnitude pulse currents.

Hanle curve is shown in Figure 2b (solid red line) yields values of τ_s = 1.4 ns, λ = 6.5 μm, and $\sqrt{p_{inj}p_{det}}$ = 0.067. The corresponding diffusion constant D is 0.034 m^2/s. We then explore the spin lifetime as a function of applied gate voltage, which tunes the polarity (electron or holes) and density of the charge carriers. The graphene channel conductivity as a function of applied back gate (V_G) is shown in Figure 2c, where the charge neutrality point can be observed at −20 V. We measure the gate dependence of the spin lifetime by carrying out Hanle precession measurements at different V_G and fitting each of these curves with eq S2. Figure 2c shows the extracted τ_s as a function of applied gate voltages, where one can observe slightly higher spin relaxation times away from the charge neutrality point. It is worthwhile to mention here that spin relaxation times observed for single layer graphene using SrO tunnel barriers are slightly better (or at least of the same order) as reported for GSVs using other tunnel barriers.[10,17,18,23,24] In addition, we have also measured spin relaxation times exceeding a nanosecond for bilayer GSV using SrO tunnel barrier at room temperature (see Supporting Information). The corresponding spin diffusion lengths as a function of gate voltage in graphene are also depicted in Figure 2d along with the graphene sheet conductivity. At higher charge carrier densities, we are able to achieve spin diffusion length of ~7 μm. Altogether, the large spin relaxation times and long spin diffusion lengths observed in graphene using SrO tunnel barriers establish that these tunnel barriers can used for high quality spin transport in graphene.

We turn our attention to measuring the absolute spin accumulation signals in graphene using dc measurements. Unlike the MR measurements, wherein a small ac excitation current is used for spin injection, we use a dc current and measure the nonlocal dc voltage signal. The schematic for the dc spin accumulation measurements is shown in the inset of Figure 3b, where a nonlocal voltage signal is measured as a function of the magnitude of dc current bias. As there is no charge current flowing into the detector electrode, the absolute nonlocal dc voltage signal ΔV_S (defined as the voltage difference of parallel and antiparallel configuration of injector and detector magnetization) is directly proportional to the net spin accumulation $\Delta \mu_S$ in the graphene ($\Delta \mu_S$ is the difference of the electrochemical potentials of majority and minority spins; $\Delta V_S = (p_{det}\Delta \mu_S)/e$, where e is the electron charge). The magnitude of ΔV_S is dependent on the interfacial quality of the ferromagnetic/graphene (e.g., contact resistance) as well as on the magnitude of the applied dc injection charge current. Ideally, one would require a smooth, pinhole-free tunnel barrier with optimum contact resistance (for enhanced spin accumulation) and which can also handle large charge current densities (to achieve higher spin accumulation) without going through electric breakdown. We have measured the current bias dependence of ΔV_S for multiple devices with graphene thickness ranging from 1−4 layers. In Figure 3, we show data from a single layer GSV device in which we have observed the highest spin accumulation signal at room temperature. For an applied dc charge current (I_{dc}) the nonlocal voltage signal V_S is recorded as a function of in-plane magnetic field, where we observe an abrupt change when the relative magnetization

direction of the injector and detector electrodes changes. The magnitude of the jump is denoted as ΔV_S, as depicted in the top curve of Figure 3a. We then measure ΔV_S as a function of I_{dc}, and the magnetic field sweeps for multiple I_{dc} are shown in the Figure 3a. Figure 3b shows the magnitude of ΔV_S, which increases with increasing I_{dc}. For the maximum applied I_{dc} of 250 μA, we observe a maximum ΔV_S of ~1.8 mV. This corresponds to an absolute spin accumulation in the graphene channel of $\mu_s = (\mu_{\uparrow\uparrow} - \mu_{\downarrow\uparrow})/2 = 7.5$ meV at the detector. As shown in Table 1, we compare our results with previous studies performing bias dependence and/or reporting large values of spin accumulation.[11−16,25] The 7.5 meV spin accumulation in the largest value reported for graphene in either the nonlocal or two-terminal local geometry. This improves upon the previous largest values for nonlocal spin transport in graphene of $\Delta V_S \sim$ 0.5 mV and $\mu_S \sim$ 1.5−2.5 meV using amorphous carbon barriers.[13] In addition, recent work using h-BN barriers reports large, bias-tunable spin injection efficiency and obtains a higher voltage switching signal of 7 mV in the two-terminal local geometry.[16] But comparing local versus nonlocal requires some care because in the local geometry, both FM electrodes are under bias and will generate spin accumulation (via spin injection/extraction) and spin drift effects may assist the spin transport. An appropriate comparison is to consider the maximum spin accumulation values of 4.1 meV cited in the h-BN study. Spin accumulation achieved using h-BN (4.1 meV) and SrO (7.5 meV) are both large and represent significant advances for the field. We also compare with the largest spin accumulation in nonlocal metallic spin valves (NiFe/MgO/Ag)[25] with voltage signals (ΔV_S = 0.22 mV) and spin accumulation (μ_S = 0.36 meV) that are smaller than reported here despite the use of short current pulses (200 μs) to permit high injection currents (3.5 mA). However, the use of pulsed currents is advantageous for generating much larger spin currents (1.5 mA in the NiFe/MgO/Ag study). It is worthwhile to consider the three metrics together because large ΔV_S is important for device architectures with voltage outputs (e.g., magnetoresistive devices), large spin current is important for spin torque, and μ_S is one of the key physical quantities that determine both. When considering all three metrics, the SrO barrier is an attractive choice.

The spin current density flowing into the detector can be calculated following the procedure developed by Takahashi et al.[7,26] As detailed in the Section 3 of the Supporting Information, the spin current density at the detector can be calculated (the detector electrode cross-section is 2.5 μm × 0.3 μm) and spin current density at the detector is plotted on the right axis of Figure 3b as a function of applied charge current. For the maximum applied charge current I_{dc} = 250 μA (charge current density of 2 × 10^9 A/m^2, with cross-sectional area 2.5 μm × 50 nm) at the injector electrode, we have achieved a spin current density of 4 × 10^6 A/m^2 at the detector. The spin current density at the detector can further be enhanced by taking several measures as discussed in the Supporting Information.

Next, we study the dependence of the spin accumulation signals on the charge carrier type and density by employing a silicon back gate. The inset to Figure 4a shows the graphene resistance as a function of applied gate voltage. We have performed these studies at 15 K. The current bias dependence of the absolute spin accumulation signals is measured at various gates and the data is shown in Figure 4a. As one can notice for higher positive bias currents (>60 μA), the electron side (V_g >

−25 V) has slightly higher spin accumulation signals as compared to the hole side (for the same I_{dc}). This is also consistent with standard MR measurements on multiple devices with SrO tunnel barriers where we see large MR signals on the electron side as compared to the hole side (see Supporting Information).

To understand the effect of interfacial contact resistance of SrO tunnel barriers on the magnitude of the spin accumulation signals, we have measured GSV devices with varying resistance area product (RA) of injector electrode. For each device, the RA product is obtained as the product of the measured three terminal injector interfacial contact resistance and area of the injector/graphene interface (i.e., product of graphene width and effective width of tunneling injector electrode which is 50 nm in our device due to angle evaporation[10]). The graphene channel length is kept identical (~2 μm) for all the devices and the back-gate voltage is held at zero. For each device spin accumulation signals are measured as a function of injector dc current before there is either some change in the interfacial contact resistance or breakdown of the tunnel barrier. In Figure 4b, we show the data with injector electrode interfacial RA product varying from 0.273 to 5.843 k$\Omega \cdot \mu$m^2. As it is evident from the data, for smaller RA product we can apply larger dc injection currents and thus achieve higher spin accumulation signals. On the other hand, for devices with higher interfacial RA product, tunnel barriers break at relatively smaller charge injection currents and prohibit achieving higher spin accumulation in graphene. Furthermore, as inferred from the slope of the curves for different RA product devices in Figure 4b, for the same applied dc charge injection current, higher RA products mean higher spin accumulation signals as opposed to electrodes with smaller RA product values. But at the same time, injector electrodes with higher RA product tunnel barriers can break at relatively smaller charge currents as compared to smaller RA product electrodes due to the larger voltage bias across the junction. This implies that there is an optimal range of injector interfacial contact resistances for achieving large spin accumulation signals in graphene. Moreover, to shed light on what happens to SrO tunnel barriers at higher charge injection currents, we carry out experiments wherein the dc spin accumulation signals and injector interfacial contact resistances are simultaneously measured. The measurement scheme is shown in the inset to Figure 4c. In Figure 4c, we have plotted spin accumulation signals (left axis) and interfacial contact resistance, R_c, (right axis) as a function of charge current applied at the injector electrode. As one can notice up to I_{dc} = 300 μA (or charge current density of 2.4 × 10^9 A/m^2) the spin accumulation grows linearly with applied injection current and the interfacial contact resistance remains constant (or unaffected). But at higher charge currents, the spin accumulation signals start to gradually decrease followed by a corresponding decrease in interfacial contact resistance. This suggests that with increasing charge current, SrO tunnel barriers start to degrade. But unlike other metal oxide tunnel barriers, SrO tunnel barriers do not go through abrupt breakdown at even charge currents as high as 500 μA (or a charge current density of 4 × 10^9 A/m^2). We speculate that it may be because our SrO barriers are uniform, pinhole-free, and amorphous that allows high biases without abrupt electric breakdown. It is worthwhile to mention here that so far, we have used constant dc injection currents for spin injection. By employing the pulsed currents, one can further reduce the Joule heating due to charge currents, and SrO tunnel barriers can

handle even higher charge current densities. Hence even larger spin accumulation can be attained in graphene using these SrO tunnel barriers. To this end, we have carried out the experiments, wherein nonlocal MR spin signals are measured after applying dc current pulses (few microseconds). The MR signals are measured using a small ac current (few μA) as explained earlier. The nonlocal MR magnitude, measured after applying gradually increasing magnitudes of pulse currents, are plotted in Figure 4d. As it is evident from Figure 4d, even after applying dc pulse currents as large as 2 mA (corresponding charge current density of 2.5×10^{10} A/m^2), the nonlocal MR signals remains constant. This further demonstrates that SrO tunnel barriers can handle high charge injection currents paving the way for realizing spin devices with stable and robust SrO tunnel barriers. This is a significant step toward our goal of achieving nonlocal spin torque magnetization switching in zero field, which has been demonstrated for metallic lateral spin valves.[27,28] Currently for graphene, there are only reports of field-assisted nonlocal spin torque switching.[29,30]

In conclusion, we have shown that MBE-grown SrO tunnel barriers in graphene spin valves are smooth, pinhole-free, and have amorphous structure. We have shown that using these SrO tunnel barriers, we can realize spin relaxation times exceeding a nanosecond for graphene on SiO$_2$ substrates which can be further improved using better substrates for graphene like h-BN. More importantly, by employing SrO tunnel barriers we have experimentally realized large spin accumulation in graphene at room temperature. By carrying out systematic studies we have shown that it is important to use an optimal range of interfacial contact resistance for achieving large spin accumulation signals in graphene. In addition, pulsed current measurements demonstrate that we can further push the limits on charge current density across these SrO tunnel barriers for attaining even higher spin accumulation. This work is a major advance for graphene spintronics where tunnel barriers play an important role in device architecture and performance.

■ ASSOCIATED CONTENT

Ⓢ Supporting Information

The Supporting Information is available free of charge on the ACS Publications website at DOI: 10.1021/acs.nano-lett.7b03543.

> A description of the procedure for fitting the Hanle spin precession data to extract spin lifetime parameters, data for spin transport in bilayer graphene using SrO tunnel barriers, calculation of the spin current density, and gate dependence of nonlocal spin signals in graphene using SrO tunnel barriers (PDF)

■ AUTHOR INFORMATION

Corresponding Author
*E-mail: kawakami.15@osu.edu.

ORCID Ⓘ
Roland K. Kawakami: 0000-0003-0245-9192

Author Contributions
‖S.S. and J.K. contributed equally to this work.

Notes
The authors declare no competing financial interest.

■ REFERENCES

(1) Han, W.; Kawakami, R. K.; Gmitra, M.; Fabian, J. *Nat. Nanotechnol.* **2014**, *9*, 794−807.

(2) Behin-Aein, B.; Datta, D.; Salahuddin, S.; Datta, S. *Nat. Nanotechnol.* **2010**, *5*, 266−270.

(3) Singh, S.; Ahmadi, A.; Cherian, C. T.; Mucciolo, E. R.; del Barco, E. d.; Özyilmaz, B. *Appl. Phys. Lett.* **2015**, *106*, 032411.

(4) Luo, Y. K.; Xu, J.; Zhu, T.; Wu, G.; McCormick, E. J.; Zhan, W.; Neupane, M. R.; Kawakami, R. K. *Nano Lett.* **2017**, *17*, 3877−3883.

(5) Tombros, N.; Jozsa, C.; Popinciuc, M.; Jonkman, H. T.; van Wees, B. J. *Nature* **2007**, *448*, 571−574.

(6) Han, W.; McCreary, K. M.; Pi, K.; Wang, W. H.; Li, Y.; Wen, H.; Chen, J. R.; Kawakami, R. K. *J. Magn. Magn. Mater.* **2012**, *324*, 369−381.

(7) Takahashi, S.; Maekawa, S. *Phys. Rev. B: Condens. Matter Mater. Phys.* **2003**, *67*, 052409.

(8) Schmidt, G.; Ferrand, D.; Molenkamp, L. W.; Filip, A. T.; van Wees, B. J. *Phys. Rev. B: Condens. Matter Mater. Phys.* **2000**, *62*, R4790−R4793.

(9) Rashba, E. I. *Phys. Rev. B: Condens. Matter Mater. Phys.* **2000**, *62*, R16267−R16270.

(10) Han, W.; Pi, K.; McCreary, K. M.; Li, Y.; Wong, J. J. I.; Swartz, A. G.; Kawakami, R. K. *Phys. Rev. Lett.* **2010**, *105*, 167202.

(11) Shiraishi, M.; Ohishi, M.; Nouchi, R.; Mitoma, N.; Nozaki, T.; Shinjo, T.; Suzuki, Y. *Adv. Funct. Mater.* **2009**, *19*, 3711−3716.

(12) Józsa, C.; Popinciuc, M.; Tombros, N.; Jonkman, H. T.; van Wees, B. J. *Phys. Rev. B: Condens. Matter Mater. Phys.* **2009**, *79*, 081402.

(13) Neumann, I.; Costache, M. V.; Bridoux, G.; Sierra, J. F.; Valenzuela, S. O. *Appl. Phys. Lett.* **2013**, *103*, 112401.

(14) Friedman, A. L.; van 't Erve, O. M. J.; Li, C. H.; Robinson, J. T.; Jonker, B. T. *Nat. Commun.* **2014**, *5*, 3161.

(15) Wen, H.; Dery, H.; Amamou, W.; Zhu, T.; Lin, Z.; Shi, J.; Žutić, I.; Krivorotov, I.; Sham, L. J.; Kawakami, R. K. *Phys. Rev. Appl.* **2016**, *5*, 044003.

(16) Gurram, M.; Omar, S.; van Wees, B. J. *Nat. Commun.* **2017**, *8*, 248.

(17) Amamou, W.; Lin, Z.; van Baren, J.; Turkyilmaz, S.; Shi, J.; Kawakami, R. K. *APL Mater.* **2016**, *4*, 032503.

(18) Singh, S.; Katoch, J.; Xu, J.; Tan, C.; Zhu, T.; Amamou, W.; Hone, J.; Kawakami, R. *Appl. Phys. Lett.* **2016**, *109*, 122411.

(19) Wu, R. J.; Topsakal, M.; Low, T.; Robbins, M. C.; Haratipour, N.; Jeong, J. S.; Wentzcovitch, R. M.; Koester, S. J.; Mkhoyan, K. A. *J. Vac. Sci. Technol., A* **2015**, *33*, 060604.

(20) Ahmed, A. S.; Wen, H.; Ohta, T.; Pinchuk, I. V.; Zhu, T.; Beechem, T.; Kawakami, R. K. *J. Cryst. Growth* **2016**, *447*, 5−12.

(21) Stecklein, G.; Crowell, P. A.; Li, J.; Anugrah, Y.; Su, Q.; Koester, S. J. *Phys. Rev. Appl.* **2016**, *6*, 054015.

(22) Sosenko, E.; Wei, H.; Aji, V. *Phys. Rev. B: Condens. Matter Mater. Phys.* **2014**, *89*, 245436.

(23) Kamalakar, M. V.; Groenveld, C.; Dankert, A.; Dash, S. P. *Nat. Commun.* **2015**, *6*, 6766.

(24) Guimarães, M. H. D.; Zomer, P. J.; Ingla-Aynés, J.; Brant, J. C.; Tombros, N.; van Wees, B. J. *Phys. Rev. Lett.* **2014**, *113*, 086602.

(25) Fukuma, Y.; Wang, L.; Idzuchi, H.; Takahashi, S.; Maekawa, S.; Otani, Y. *Nat. Mater.* **2011**, *10*, 527−531.

(26) Takahashi, S.; Maekawa, S. *Sci. Technol. Adv. Mater.* **2008**, *9*, 014105.

(27) Yang, T.; Kimura, T.; Otani, Y. *Nat. Phys.* **2008**, *4*, 851−854.

(28) Zou, H.; Ji, Y. *J. Magn. Magn. Mater.* **2011**, *323*, 2448−2452.

(29) Lin, C.-C.; Penumatcha, A. V.; Gao, Y.; Diep, V. Q.; Appenzeller, J.; Chen, Z. *Nano Lett.* **2013**, *13*, 5177−5181.

(30) Lin, C.-C.; Gao, Y.; Penumatcha, A. V.; Diep, V. Q.; Appenzeller, J.; Chen, Z. *ACS Nano* **2014**, *8*, 3807−3812.